

GPU Performance of an Entropy-Stable Discontinuous Galerkin Euler Solver with Non-Conservative Terms

Henry Waterhouse^a, Maciej Waruszewski^b, Lucas C. Wilcox^c, Timothy Warburton^d,
Francis X. Giraldo^{a,c,*}

^a*Department of Applied Mathematics, University of California, Santa Cruz, CA*

^b*Sandia National Laboratories, Albuquerque, NM*

^c*Department of Applied Mathematics, Naval Postgraduate School, Monterey, CA*

^d*Department of Mathematics, Virginia Tech, Blacksburg, VA*

Abstract

The entropy-stable discontinuous Galerkin method for compressible Euler equations with buoyancy is implemented on graphics processing unit (GPU) hardware. We measure the performance of the solver on three-dimensional problems: the rising thermal bubble and the baroclinic instability in a channel. On NVIDIA A100 hardware, the solver achieves nearly 70% of 64-bit floating-point peak performance for the most computationally expensive kernel (volume terms) and significantly reduces the computational overhead typically incurred by two point entropy-stable fluxes in the volume terms. We also present impressive strong and weak scaling performance of the solver and compare to a highly-optimized central processing unit (CPU) code showing that the GPU kernels are a factor of $10\times$ faster and better than $13\times$ more energy efficient than the CPU code. We also show that the solver achieves the expected $2\times$ speedup when run at 32-bit floating-point peak performance. We discuss the different modifications that we implemented to reach the final form of the GPU implementation and measure the performance gain of each of the implementation strategies ranging from reduction in complex operations and memory traffic as well as load balancing. We also extend symmetry-based flux savings to the non-symmetric gravity term, preserving nearly the full factor-of-two speedup achieved for the symmetric flux.

Keywords: atmospheric model, balance laws, baroclinic instability, buoyancy, compressible Euler equations, discontinuous Galerkin, entropy-stable method, flux-differencing, nonhydrostatic, numerical weather prediction, rising thermal bubble, Runge-Kutta method

1. Introduction

The construction of accurate, stable, and efficient dynamical cores in atmospheric modeling remains a topic of interest despite the volume of literature on this subject. Most (perhaps all) existing atmospheric models require some form of regularization to maintain stability. Typically, this regularization has come in the form of hyper-diffusion (see, e.g., [21, 30]). Although this idea has been improved to make it more adaptive (see, e.g., [27, 23]),

*Corresponding author

some tuning is still required when the model resolution is modified. Discontinuous Galerkin (DG) methods offer many advantages in geophysical fluid dynamics modeling thanks to their: (1) high-order accuracy, (2) stability due to the use of Riemann solvers (essentially augmenting the numerics with analytic information from the method of characteristics), and (3) the local element-wise construction which offers unmatched parallelization (i.e., efficiency) [29, 1, 2]. The main Achilles heel of these methods has been: (i) stability at high-order and (ii) time-step restriction. The stability issue has been resolved thanks to entropy-stable methods (see, e.g., [51, 52, 10, 17, 33, 20, 34, 40, 15, 18, 14, 13, 44, 55, 49]) which seek to construct the correct numerical flux that either conserves entropy (entropy-conservative methods) or dissipates it (entropy-dissipative or entropy-stable methods); this is achieved by deriving the numerical flux for the associated entropy equation that achieves these goals. The time-step issue has been ameliorated, to some degree, by implicit methods (see, e.g., [43, 23, 56]). These last two points solve the stability and time-step restriction, leaving the efficiency issue to address (DG resolves the accuracy condition; see, e.g. [28, 32, 22]). Entropy-stable discontinuous Galerkin (ESDG) methods are expensive to compute due to the use of two-point fluxes (see [17]). Therefore, it is the main objective of this paper to show how to construct efficient ESDG methods on modern high-performance computing architectures, i.e., graphics processing units (GPUs); Ranocha et al. [41] tackled many of these issues on the CPU. We aim to show how each optimization we apply improves the efficiency, thereby developing a roadmap for constructing efficient GPU code for various applications, although here we focus on the Euler equations with buoyancy. The challenge of including buoyancy in the Euler equations is that the resulting system of nonlinear partial differential equations no longer forms a system of conservation laws but rather a system of balance laws with non-conservative terms that must be handled carefully; to this end, we follow the ESDG method presented in [55]. To our knowledge, the only published work on the GPU performance of ESDG has exclusively focused on the shallow water equations [58, 61]; our manuscript represents the first work on ESDG for the Euler equations that focuses on GPU optimization – our aim is to demonstrate the effect that various optimizations have on performance such as reductions in complexity and memory usage.

It is important to note that, in the last two decades, a large volume of work has appeared on GPUs for the Euler equations, e.g.. [16, 35, 37, 48, 47, 59, 19, 1, 2, 62, 26, 31, 46, 6, 54, 11, 12, 36, 60, 50, 56]. A smaller collection focuses on the GPU implementation of discontinuous Galerkin methods for the shallow water, e.g., [61, 58] and Euler, e.g., [48, 47, 19, 1, 2, 31, 54, 11, 12, 36, 56] equations. From this list, only two papers focus on the GPU implementation of entropy-stable discontinuous Galerkin methods for the shallow water equations and none for the Euler equations. This literature review shows that although a rather large volume of work has appeared on entropy-stable discontinuous Galerkin methods, very few (to none) have appeared on the GPU implementation of these methods. Our goal is to fill this important gap in the literature because, without improving performance, ESDG methods (as good as they are) run the risk of falling out of favor to due their computational cost.

The remainder of the paper is organized as follows: Sec. 2 describes the form of the Euler equations that we use in this study which includes the effect of buoyancy and Sec. 3 presents the entropy-stable discontinuous Galerkin discretization. Section 4 is the heart of the paper where we describe the GPU performance of the algorithm where Sec. 4.1 contains

the discussion on the optimizations we implemented to improve performance and Secs. 4.2 and 4.3 contain the single and multi-GPU performance results. We test our algorithm on three-dimensional test cases in Sec. 5 and conclude the paper in Sec. 6.

2. Governing Equations

This study considers flow governed by the time-dependent compressible Euler equations. Let $\Omega \in \mathbb{R}^3$ be a fixed domain in 3D with boundary Γ . Let us denote the fluid density, velocity vector, and total energy by ρ , $\mathbf{u} = u_i$ ($i = 1, 2, 3$), and e , where $e = c_v T + \frac{1}{2} \mathbf{u} \cdot \mathbf{u} + \phi$ with c_v denoting the specific heat at constant volume, T is temperature, and $\phi = gz$ is the geopotential with g being the gravitational constant. The Euler equations are defined in conservation form as follows

$$\frac{\partial \rho}{\partial t} + \nabla \cdot \mathbf{U} = 0 \quad (1a)$$

$$\frac{\partial \mathbf{U}}{\partial t} + \nabla \cdot \left[\frac{1}{\rho} \mathbf{U} \otimes \mathbf{U} + P \mathbf{I}_3 \right] + \rho \nabla \phi + \boldsymbol{\Omega} \times \mathbf{U} = 0 \quad (1b)$$

$$\frac{\partial E}{\partial t} + \nabla \cdot \left[\left(\frac{E + P}{\rho} \right) \mathbf{U} \right] = 0 \quad (1c)$$

where $\mathbf{U} = \rho \mathbf{u}$ is the momentum, $E = \rho e$ is the density total energy (which includes kinetic, internal, and potential energies), $\boldsymbol{\Omega}$ is the rotation rate contributing to the Coriolis effect, P is the pressure defined as

$$P = (\gamma - 1) \left(E - \frac{1}{2\rho} \mathbf{U} \cdot \mathbf{U} - \rho \phi \right),$$

with $\gamma = \frac{c_p}{c_v}$ is the specific heat ratio, and \mathbf{I}_3 is the rank-3 identity matrix

A few remarks on Eqs. (1), ignoring the geopotential (buoyancy) and Coriolis terms in momentum results in a conservation law. The buoyancy and Coriolis terms are what distinguishes the standard Euler equations in computational fluid dynamics from those required in geophysical fluid dynamics and results in a balance law. It is the non-conservative buoyancy term in particular that causes us to construct specialized entropy-stable discretizations as outlined in the next section.

3. Numerical Method

The entropy-stable discontinuous Galerkin discretization this study considers is detailed in [55]. Here we provide a brief description of the method with a focus on the operations the computational kernels implement.

The domain is divided into a finite number of non-overlapping elements which make up the computational domain. Each element is mapped to the hexahedral reference element containing the tensor-product of $(N + 1)^3$ Legendre-Gauss-Lobatto (LGL) quadrature nodes, where N is the polynomial-order of approximation. The discrete state vector stores the approximate solution at these nodes and all integrals are evaluated using the associated quadrature weights (to increase computational efficiency by avoiding projections between

interpolation and integration nodes). For each element, the semi-discrete form of the entropy-stable discontinuous Galerkin discretization is given as

$$\frac{dq}{dt} = \underbrace{h - \sum_{j,k=1}^3 (G_{jk} (D_j \circ F_j) - (F_j \circ D_j^T) G_{jk}) \mathbf{1}}_{\text{volume term}} - \underbrace{\sum_{j,k=1}^3 M^{-1} M^s G_{jk}^s F_j^*}_{\text{surface term}}, \quad (2)$$

where q is a vector of the state approximated at the nodes on the element; h is a vector containing a source evaluated at the nodes; G_{jk} is geometric factor diagonal matrix containing the metric derivatives of the k -th direction reference coordinate with respect to the j -th direction spatial coordinate; D_k is the k -th reference direction nodal differentiation matrix; F_j is the j -th spatial direction two-point flux matrix that ensures entropy conservation and F_j^* is the corresponding entropy-dissipative flux defined as the entropy-conservative flux with additional dissipation included; $\mathbf{1}$ is a vector of ones; M is the Jacobian weighted LGL quadrature based diagonal element mass matrix; G_{jk}^s is the geometric factor diagonal matrix for the element surface nodes; M^s is the Jacobian weighted LGL quadrature based diagonal surface mass matrix. The volume and surface terms are applied in a matrix-free way exploiting the tensor product structure of the differentiation matrices. For example, only an $N_q \times N_q$ matrix will need to be loaded to apply each derivative, where $N_q = N + 1$ is the number of quadrature points in each dimension of the reference element. The elements are connected together through the calculation of the surface flux vector, which requires state values from the current element (the minus side of the surface) and the neighboring elements (the plus side of the surface). Entropy stability is ensured by evaluating the flux using a specific two-point flux formula which allows one to prove discrete entropy stability [55]. For the volume kernels, we use the entropy-conserving two-point flux described in [55] (Eq. 76); for the surface flux we use the same entropy-conserving flux in addition to the matrix dissipation outlined in [55] (Eq. A.1). The entropy-conserving flux is quite computationally intensive since its construction requires mean values, jump values, logarithms, and reciprocals. The matrix dissipation is somewhat computationally intensive because of its need to perform the matrix diagonalization of the Jacobian matrix, akin to a Roe Riemann solver [45]. As detailed in Section 4, this is done exploiting symmetry and the tensor product structure to minimize the amount of computations.

We discretize in time using the fourth-order, low-storage, Runge–Kutta scheme [9]. The elements of the two-point flux matrices F_j and vectors f_j depend on the state and need to be recomputed at each stage. This accounts for a significant portion of the floating-point operations performed in the volume and surface kernels.

4. Performance Analysis

4.1. GPU optimizations

DG methods operate on a set of independent elements that only communicate through surface fluxes at the boundaries. Most of the work is done inside an element, in what is usually referred to as the volume term, that is well suited to GPU optimizations. The GPU thread hierarchy is organized into thread blocks. Threads within a block can cooperate,

but each thread block is scheduled independently. The first step in GPU optimization is to determine an efficient mapping of computational work to GPU threads. DG methods provide an obvious distribution methodology: each element is represented by a thread block, with each thread within that block representing a single degree-of-freedom (DOF) within the computational element.

Along with this distribution of work, there are many optimizations to be made to the kernel itself. We build on the efficient two-point flux formulation of [41], which benchmarked serial central processing unit (CPU) performance, and extend it to the GPU. Figure 1 shows the cumulative effect of each optimization step, culminating in a total speedup of $7.3\times$ over the baseline GPU kernel. We discuss the most significant optimizations below.

The two-point flux used in flux-differencing methods (e.g., entropy-stable and kinetic-energy-preserving methods) is evaluated between every pair of quadrature nodes along each coordinate direction, requiring $O(N_q)$ evaluations per DOF per direction. The high number of evaluations of this flux function makes it crucial to avoid as many expensive operations within the function as possible. Two classically expensive operations in high performance computing are divisions and logarithms, both of which feature prominently in entropy stable fluxes. Logarithms are particularly costly in 64-bit floating-point precision on GPUs, where transcendental functions lack dedicated hardware support [39]. A main source of the divisions is computing primitive variables (e.g., $u = \rho u / \rho$). We limit this bottleneck by precomputing these once per thread instead of as needed in the flux. The logarithms appear in the form of logarithmic means. We adopt the efficient logarithmic mean formulation of [42], which reduces divisions with Horner’s rule. We further rewrite the logarithmic mean so that it depends on $\log(a)$ and $\log(b)$ individually rather than on $\log(\frac{a}{b})$ allowing the logarithms to be computed once per thread and reused across all evaluations. These changes make each evaluation of the two-point flux cheaper, but we can also lower the total number of two-point fluxes by using symmetry.

Exploiting symmetry for the more straightforward case of standard Euler equations, where the entropy stable flux is built from symmetric averages, is described in [42]. Here, we encounter two additional complications. The first one is that the gravity term results in non-symmetric terms added to the entropy stable flux. The second one is that the standard CPU way of computing only the necessary two-point fluxes leads to load imbalance on GPUs. The first problem comes from the momentum flux. We show this by first defining:

$$\{\{a\}\} = \frac{a^+ + a^-}{2}, \quad \{\{a\}\}_{\log} = \frac{a^+ - a^-}{\log(a^+) - \log(a^-)}, \quad \llbracket a \rrbracket = a^+ - a^- \quad (3)$$

and then stating the form of the momentum flux:

$$(\rho u_k)^* \{\{u_m\}\} + \delta_{mk} \left(p^* + \frac{1}{2} \hat{\rho} \llbracket \phi \rrbracket \right), \quad (4)$$

where

$$\hat{\rho} = \frac{\{\{b\}\} \{\{\rho\}\}_{\log}}{b^-} \quad (5)$$

contains the one-sided $b^- = \rho^- / (2p^-)$. Under an $i \leftrightarrow j$ swap, the jump $\llbracket \phi \rrbracket$ flips sign and

b^- becomes b^+ , so the gravity term transforms as $\frac{1}{2}\hat{\rho}[\phi] \rightarrow -\frac{1}{2}\hat{\rho}[\phi] \cdot \frac{b^-}{b^+}$, which is not a simple sign flip when $b^- \neq b^+$. We handle this by decomposing the momentum flux into a symmetric part $S = (\rho u_k)^* \{u_m\} + \delta_{mk} p^*$ and the gravity contribution $G = \frac{1}{2}\hat{\rho}[\phi]$. For each quadrature pair, the flux is computed once and the partner node’s gravity contribution is obtained by a single scaling: $G \rightarrow -G \cdot b^-/b^+$. The density and energy components remain fully symmetric and require only a sign flip. This preserves nearly all of the factor-of-two savings from the half-sweep while correctly handling the gravitational coupling. The second challenge of exploiting symmetry comes from GPU threading. A naive assignment of work where thread i computes two-point fluxes $F_{i,j}$ for $j > i$ leads to load imbalance. We can handle this by making thread i compute $F_{i,1+(i+l-2) \bmod N_q}$ for $l = 2, \dots, N_l$ where

$$N_l = \begin{cases} \left\lfloor \frac{N_q}{2} \right\rfloor + 1 & \text{for even } N, \\ \frac{N_q}{2} + 1 & \text{for odd } N \text{ and } i \leq \frac{N_q}{2}, \\ \frac{N_q}{2} & \text{for odd } N \text{ and } i > \frac{N_q}{2}, \end{cases} \quad (6)$$

and $\left\lfloor \frac{N_q}{2} \right\rfloor$ denotes integer division. This assignment of two-point flux computations still accounts for every combination where $j > i$, while leading to substantially better load balancing. For even polynomial orders, every thread is doing the same number of flux computations, which is optimal. For odd polynomial orders, half the threads do one more iteration, which is still much better than the naive way. A modification of this approach is to keep the loop bounds constant at $\frac{N_q}{2} + 1$ and appropriately apply a weight of 1/2 to antipodal pairs when the polynomial order is odd. The benefit of this being that each thread performs the same number of loop iterations which can avoid potential issues with syncing threads. The results in this code use the weighting approach, but we include the description of the indexing approach since it illustrates for which pairs the antipodal double counting occurs.

Figure 1 shows that the combination of primitive and logarithmic precomputation, the efficient logarithmic mean formulation, and the exploitation of symmetry account for the majority of the total $7.3\times$ speedup. In this figure, N denotes the polynomial degree of the basis function for each direction and the number of elements in the mesh are defined by $N_e = K \times 2^{3L}$ where $K = K_x \times K_y \times K_z$ where K_j denotes the number of base elements along direction j and L denotes the refinement level of the mesh. Unless specifically stated, the test cases are run with only one base element ($K = 1$). Along with the major speedups above, we applied many GPU targeted optimizations. The two-point flux involves communication across the entire element. This means that nodes are regularly accessing other nodes’ information, meaning the memory efficiency and layout are important. A key aspect of this is placing the state variables, the auxiliary variables, and other regularly accessed quantities like the precomputed logarithms and differentiation matrix in shared memory. This gives the whole element quick access to other nodes’ values. Our baseline kernel was launched once per direction, loading shared memory each time; fusing all three directions into a single launch eliminates these redundant loads. We compute the contravariant flux directly rather than forming a 3×5 flux matrix and then contracting, which reduces the total number of operations in the inner loop. Finally, we made many standard optimizations such as

precomputing reciprocals to reduce the total number of divisions and removing redundant loads or operations from loops.

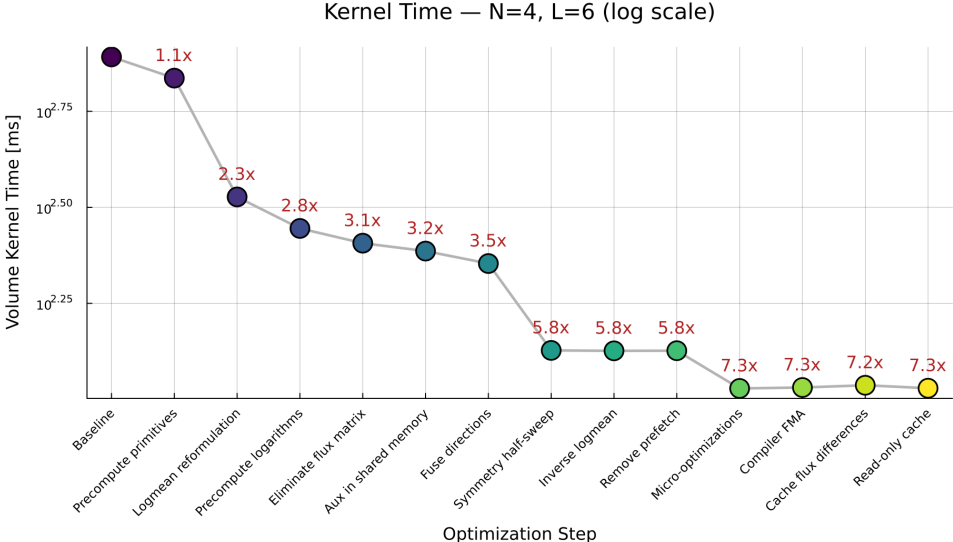


Figure 1: Total volume kernel GPU time per timestep for each cumulative optimization step. Measured on an NVIDIA A100 SXM4 40GB with $N = 4$, $L = 6$, 64-bit floating-point precision, using NVIDIA Nsight Compute.

4.2. Single-GPU

Our optimized volume kernel is in the compute bound regime for polynomial order $N \geq 3$, achieving nearly 70% of the roofline ceiling. We can show this by analyzing a roofline plot of the kernel, a performance model introduced in [57]. We plot the result in Figure 2 with the results for all refinement levels on the left and the most saturated results on the right. The horizontal axis is arithmetic intensity, which is a ratio of floating point operations to bytes transferred. The vertical axis is performance, which is the number of floating point operations per second. As we increase the polynomial order, denoted by marker shape, our data points move to the right since there is more work to be done per piece of data on the hardware. As we increase the refinement level, denoted by marker color, we increase the amount of parallel work, pushing performance upward. We observe a slight leftward shift at higher refinement levels due to less optimal cache usage for larger problem sizes. We also see diminishing peak performance for increasing polynomial order beyond $N = 3$ which is attributable to larger thread block sizes reducing occupancy. DG methods are typically run at high orders ($N \geq 3$) and the plot shows that all such cases are compute-bound. What we can infer from this plot is: (i) the volume kernel is well-suited to GPU parallelization since it is not memory bandwidth-limited at typical polynomial orders and (ii) our code can take advantage of rapidly evolving GPU hardware since compute-bound kernels benefit from FLOP/s increases.

A full step of our code involves 3 parts: the volume kernel, the surface kernel, and the Runge-Kutta (RK) time-stepping kernel; we have only discussed the volume kernel so

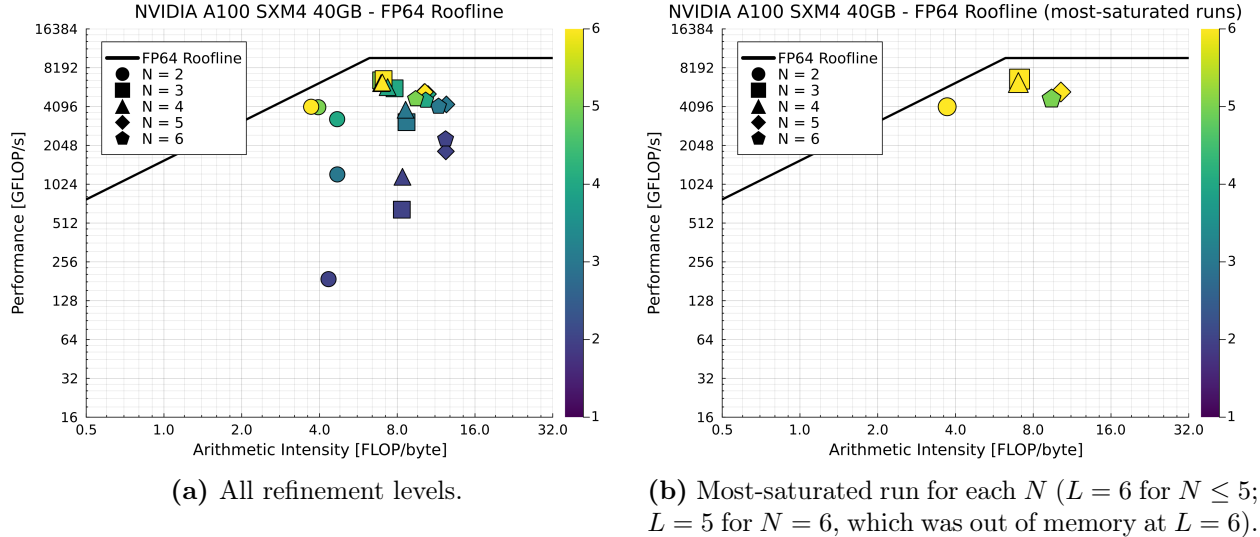


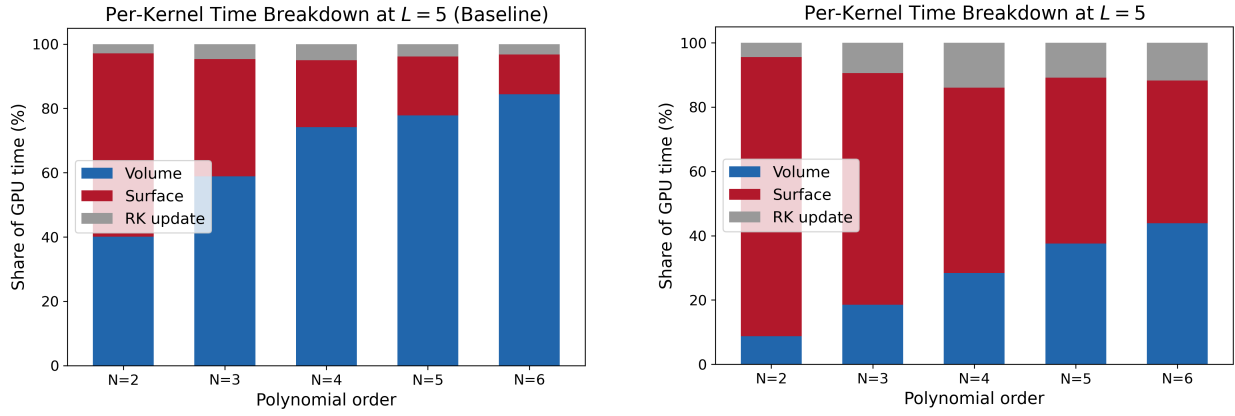
Figure 2: Roofline plots of the optimized volume kernel on an NVIDIA A100 SXM4 40GB (peak FP64: 9,746 GFLOP/s, peak bandwidth: 1,560 GB/s). Marker shape denotes polynomial order N and color denotes refinement level L (dark to light: coarse to fine). (a) shows every (N, L) configuration; (b) restricts to the most refined mesh available for each polynomial order, isolating the saturated-GPU regime.

far. Figure 3 shows the per-kernel share of GPU time before and after our volume-kernel optimizations. In panel (a), the volume kernel is the bottleneck for $N \geq 3$ and dominates total runtime; in panel (b), after optimization, the surface kernel becomes the dominant cost across all tested polynomial orders. The optimized volume kernel therefore addresses the cost issue of entropy-stable DG, and future optimizations will likely need to target the surface kernel, which is memory-bound and so will require different techniques than those used here.

Inspired by [3] we show the throughput as a function of the number of elements in Fig. 4; on the horizontal axis we vary the number of three-dimensional elements on a single GPU while on the vertical axis we report on the number of elements evaluated in one time-step per wallclock second (in thousands). The higher values for the lowest degree polynomial ($N = 2$) show that even at 256k elements we have not yet fully saturated the device. In contrast, for the highest degree polynomial ($N = 6$) we are able to fully saturate the device at 4k elements. This difference in number of elements needed for saturation can be attributed to elements at higher polynomial orders containing more degrees of freedom and, therefore, having more work per degree of freedom (i.e., higher arithmetic intensity). From this plot, we can see for example that if you had a problem that had 128k elements and $N = 4$ polynomials, the optimal number of GPUs to deploy would be 4 (resulting in 32k elements per GPU) since each GPU is fully saturated at this point. If we used more GPUs, the results would shift left on the curve thereby underutilizing each device.

4.3. Multi-GPU

The preceding section focused on performance analysis on one GPU, we now move on to multi-GPU strong and weak scaling results. Before discussing the scaling results, it is



(a) Per-kernel share of GPU time at $L = 5$ with baseline volume kernel.

(b) Per-kernel share of GPU time at $L = 5$ with optimized volume kernel.

Figure 3: Percent of total GPU time for the three main kernels at refinement level $L = 5$. (a): the unoptimized volume kernel dominates for $N \geq 3$. (b): after optimization, the surface kernel becomes the dominant cost across the tested polynomial orders.

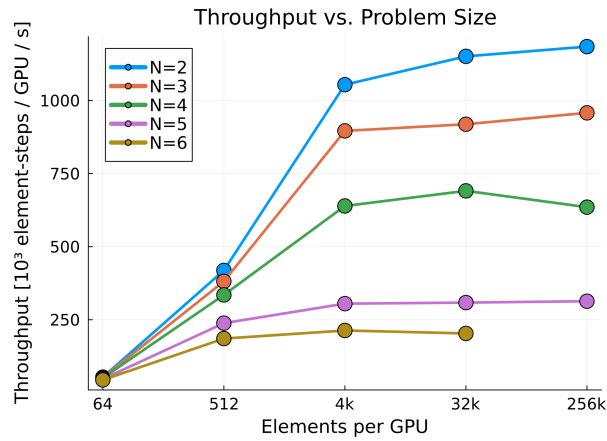


Figure 4: Single-GPU throughput in thousands of element–time-steps per second as the number of elements grows ($K = 1$ base mesh refined L times, so element count = 2^{3L}). Each curve corresponds to one polynomial order; the flattening of each curve marks the element count at which the GPU is saturated for that order.

worth saying a few words describing the Message Passing Interface (MPI) strategy. We assign each MPI rank a single GPU and distribute elements to these GPUs using `p4est`; more information on the Morton space-filling curve based distribution method can be found in [7]. We implement the overlapping communication strategy of [29]. This entails posting non-blocking sends and receives for the boundary data at the beginning of each timestep so that the communication overlaps with both the volume flux and the intra-processor surface integrals. The algorithm then waits for the communication to finish and computes the inter-processor surface integrals. For portability we use host-based MPI rather than direct CUDA-Aware MPI; all scaling results below are obtained with this configuration.

Strong scaling fixes the problem size and increases the processor count. For this test, we ran the rising bubble test case with 4th order polynomials and 6 refinement levels ($2^6 = 64$ elements in each direction) for 1000 time steps. We show the results in the left panel of Figure 5. The left panel shows that speedup falls below ideal as GPU count increases due

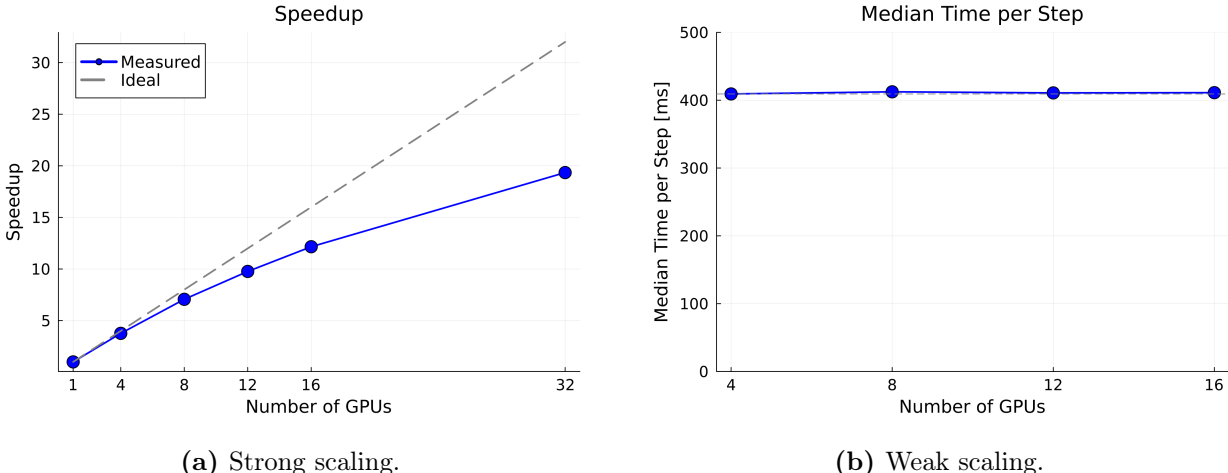


Figure 5: Multi-GPU scaling of the rising-bubble benchmark at $N=4$, $L=6$ on NVIDIA A100 GPUs. (a) strong-scaling speedup on 1–32 GPUs for a fixed 32.8M-DOF problem, against ideal linear speedup. (b) weak-scaling median time per step as the element count grows with the GPU count (one identically discretized element per device).

to communication overhead and progressive underutilization of each GPU. At 32 GPUs, parallel efficiency drops to 60%, suggesting that a better use of the hardware is to match problem size to processor count, which we explore below.

For weak scaling, we increase both problem size and number of processors simultaneously. For this test we once again used 4th order polynomials and 6 refinement levels, but this time we increased the number of elements to coincide with the number of processors – the results are shown in the right panel of Figure 5. For example, the run with 4 processors has 4 elements each with 4th order polynomials and 6 refinement levels. When we increase to 8 processors, we now have the same setup but with 8 elements. This is representative of a real world use case where you would decide the number of processors to use based on the size of your problem. We see from our results that our code maintains approximately the same time per step for increasing GPUs and problem sizes. This is an ideal result that shows the time to solution for a large problem can be approximately the same as that of a smaller problem

as long as we properly allocate computational resources.

The above weak scaling test is “ideal” in that our refinements are each in separate elements and the number of elements aligns with the number of processors. To stress our code with a less ideal scenario, we use one coarse element and increase refinement level and processors to keep the problem size per processor constant. The results of this are shown in the left panel of Figure 6.

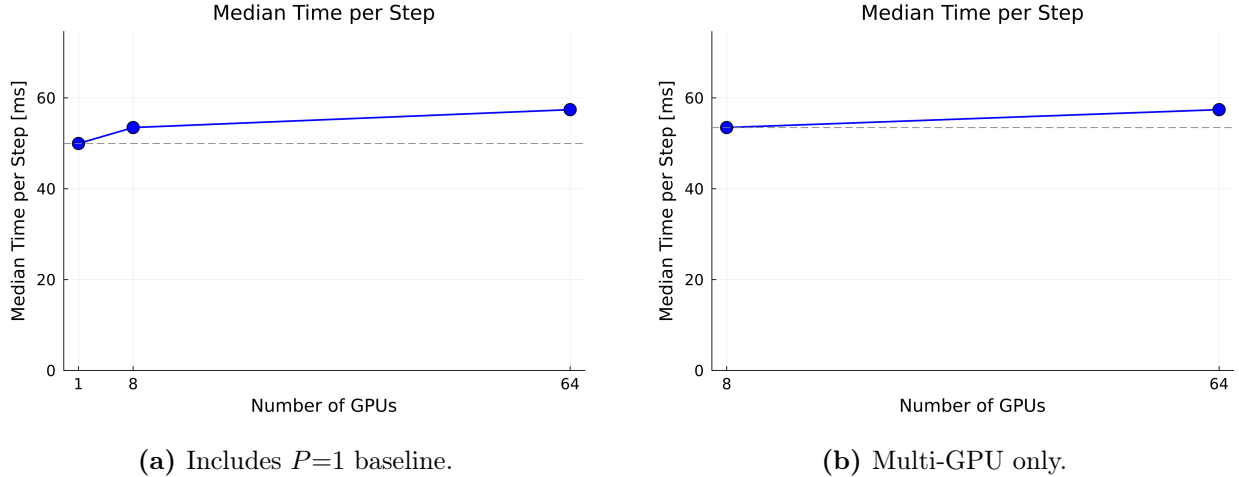


Figure 6: Weak-scaling median time per step where the GPU count grows with the refinement level (a single coarse element is subdivided so each GPU holds identical work: $L=6$ at 8 GPUs, $L=7$ at 64 GPUs). (a) includes the $P=1$ baseline; the jump from 1 to 8 GPUs largely reflects the absence of inter-GPU communication in the serial run rather than true weak-scaling loss. (b) baseline shifted to $P=8$ so only multi-GPU effects are visible.

The drawback of this test is that the exponential increase in the necessary GPUs to scale with the refinement limits the data we can gather since we don’t have access to 512 GPUs. Because of this we include the single GPU case in the left panel of Figure 6, but clearly the single GPU won’t have communication overhead and we see a large drop in efficiency from 1 to 8 GPUs. We remove this single-GPU data point in the right panel of Figure 6 and see that the efficiency drop between the multi-GPU runs is not as significant.

4.4. GPU versus CPU

We next compare the performance of the GPU code with the CPU code. For the CPU code, we use the NUMA model [24, 23]. For the comparison, we use the exact same grid size, time-step, and numerical methods (entropy-stable DG with explicit LSRK time-stepping). Although the GPU and CPU codes are rather different (the GPU code is written in Julia [5] using CUDA.jl [4] with MPI.jl [8] and the CPU code is written in modern Fortran using Message Passing Interface), both codes use `p4est` [7] to generate meshes in parallel and have been designed to run optimally on their specific device of choice (e.g., see NUMA results on CPUs in [38]). For the comparison, we run the codes on the Delta computer at the National Center for Supercomputing Applications which has 400 NVIDIA A100 GPUs and 256 AMD EPYC 7763 Milan nodes; in the results below we report the CPU result for 2 sockets per node so effectively Delta has 128 of the AMD Milan 2-socket nodes. The thermal design

Hardware	No. Devices	Time-to-Solution (s)	Energy Consumption (MJ)	R_{time}	R_{energy}
A100	4	110	0.18	11.28	15.79
Milan	4	1241	2.78	–	–
A100	8	60	0.19	9.88	13.84
Milan	8	593	2.66	–	–
A100	16	30	0.19	10.73	15.03
Milan	16	322	2.89	–	–

Table 1: Comparison of time-to-solution, energy consumption, and the ratios between the A100 (GPU) and the AMD Milan (CPU).

power (TDP) of the A100 is 400 Watts while that for the AMD (7763) node (with 64-cores) is 280 Watts (we multiply this TDP by 2 since each node has 2 sockets) ¹ We summarize the comparison between GPU and CPU hardware in Table 1, where energy consumption is calculated as follows

$$\text{Energy Consumption (MJ)} = \text{Time-to-solution (s)} * \text{TDP (Watts=Joules/s)} / 10^6.$$

R_{time} denotes the ratio in time-to-solution between the CPU and GPU for the same number of nodes (as described above). R_{energy} denotes the ratio in energy consumption between the CPU and GPU. R_{time} shows that the GPU is $\sim 10\times$ faster than the CPU. To be more specific, this result shows that to achieve the same time-to-solution as one NVIDIA A100 GPU, we would need 10 dual socket AMD Milan nodes (1280 AMD cores). However, since energy consumption is an important consideration, we also compute R_{energy} which shows that the GPU is at least $13\times$ more efficient than the CPU.

5. Simulation Results

In this section, we demonstrate that the GPU efficient algorithms described in Sec. 4 yield good solutions for geophysical fluid dynamics problems of interest. Below, we show results for a three-dimensional discontinuous rising thermal bubble and for a three-dimensional baroclinic instability in a channel. For both test cases, we show results for 64-bit and 32-bit floating-point precision and for the baroclinic instability test we compare the ESDG solution against the most mature nonhydrostatic atmospheric model we have in our computational arsenal.

5.1. Rising Bubble

We run a full 3D simulation of a rising thermal bubble [55]. Our domain is $x \in [-1000, 1000]$ m (periodic), $y \in [-1000, 1000]$ m (periodic), and $z \in [0, 2000]$ m (reflecting).

¹We make the assumption that both the GPU and CPU devices are fully engaged thereby using the TDP as their measure of energy consumption, although this may not necessarily be the case.

We start the bubble in two different ways. The first, shown in Figure 7, is a sharp discontinuity defined by:

$$\delta\theta = \begin{cases} \frac{1}{2} & r \leq r_c \\ 0 & \text{otherwise} \end{cases} \quad (7)$$

where $\delta\theta$ is the potential temperature perturbation, $r = |\mathbf{x} - \mathbf{x}_c|$, $r_c = 250$, and $\mathbf{x}_c = (0, 0, 260)$. This places a spherical bubble of radius 250 m centered at (0, 0, 260) m. This is a sharp profile that immediately jumps from no to full perturbation. The second configuration [25] keeps everything the same, but smooths out the initial perturbation as:

$$\delta\theta = \begin{cases} \frac{1}{2} \frac{(1 + \cos(\pi \frac{r}{r_c}))}{2} & r \leq r_c \\ 0 & \text{otherwise.} \end{cases} \quad (8)$$

For both of these configurations, we run with 64-bit and 32-bit precision with $N = 4$ polynomial order and $L = 6$ refinement level on one coarse element resulting in a total DOF count of 32,768,000 ($N_e = (2^6)^3 = 262,144$ and $N_p = N_e(N + 1)^3 = 32,768,000$). We ran this simulation on 8 GPUs with a Courant number (C) of 0.5 and a resultant timestep of $\Delta t \approx 8.18 \times 10^{-3}$ s. We present a slice of the potential temperature results at $y = 0$ for three different timesteps. We see that the 64-bit precision results mostly maintain large-scale symmetry while the 32-bit precision results diverge slightly over time. Due to the minimal amount of numerical dissipation, the solution may lose symmetry due to non-symmetric rounding errors. (For example, the symmetry in Figure (3) of [55] was obtained by ensuring rounding errors were made symmetrically.) Despite these differences in symmetry, the practical benefit of 32-bit precision is substantial: The timing results, summarized in Table 2, show that 32-bit precision consistently yields a $2\times$ speedup across both initial conditions. Changing the precision type is as easy as passing an argument to the run script and requires no other configuration.

Table 2: Timing results for the rising bubble simulation with $N = 4$, $L = 6$ (32,768,000 DOF), and 8 GPUs.

Perturbation	Precision	Total Time [s]	Speedup
Sharp (7)	64-bit	6622.03	—
	32-bit	3070.25	2.16×
Smooth (8)	64-bit	6556.21	—
	32-bit	3037.88	2.16×

5.2. Baroclinic Instability

We run a 3D baroclinic wave test case following the benchmark from [53]. The domain is $x \in [0, 40000]$ km (periodic), $y \in [0, 6000]$ km (reflecting), and $z \in [0, 30]$ km (reflecting). The background state is a balanced zonal wind, which is then overlain with a Gaussian perturbation which triggers an instability. We run this simulation with $N = 4$ polynomial

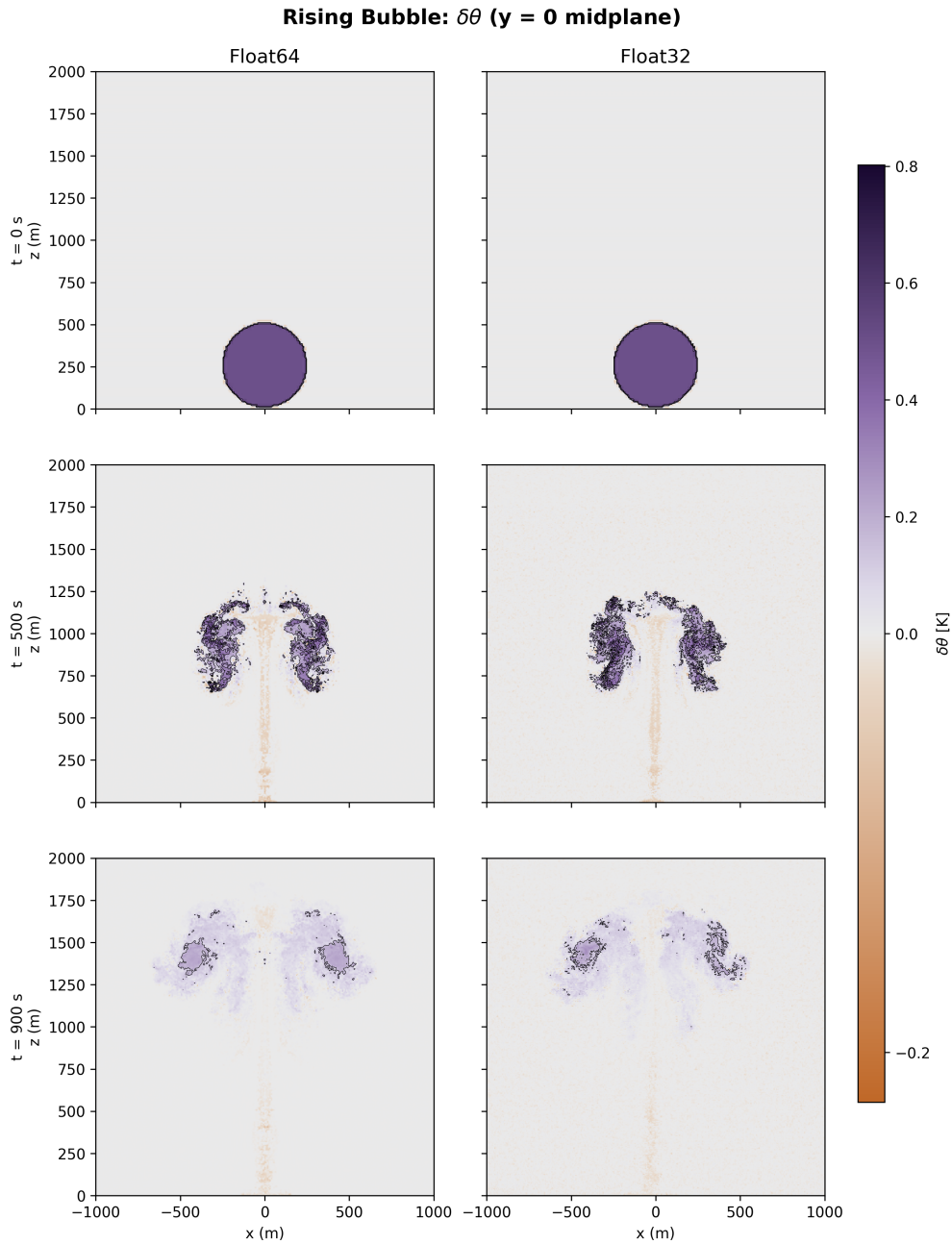


Figure 7: Slices of simulation results for potential temperature at $y = 0$ with $N = 4$, $L = 6$, and one coarse element in 64-bit (left) and 32-bit (right) precision. This simulation uses the sharp initial perturbation defined in (7).

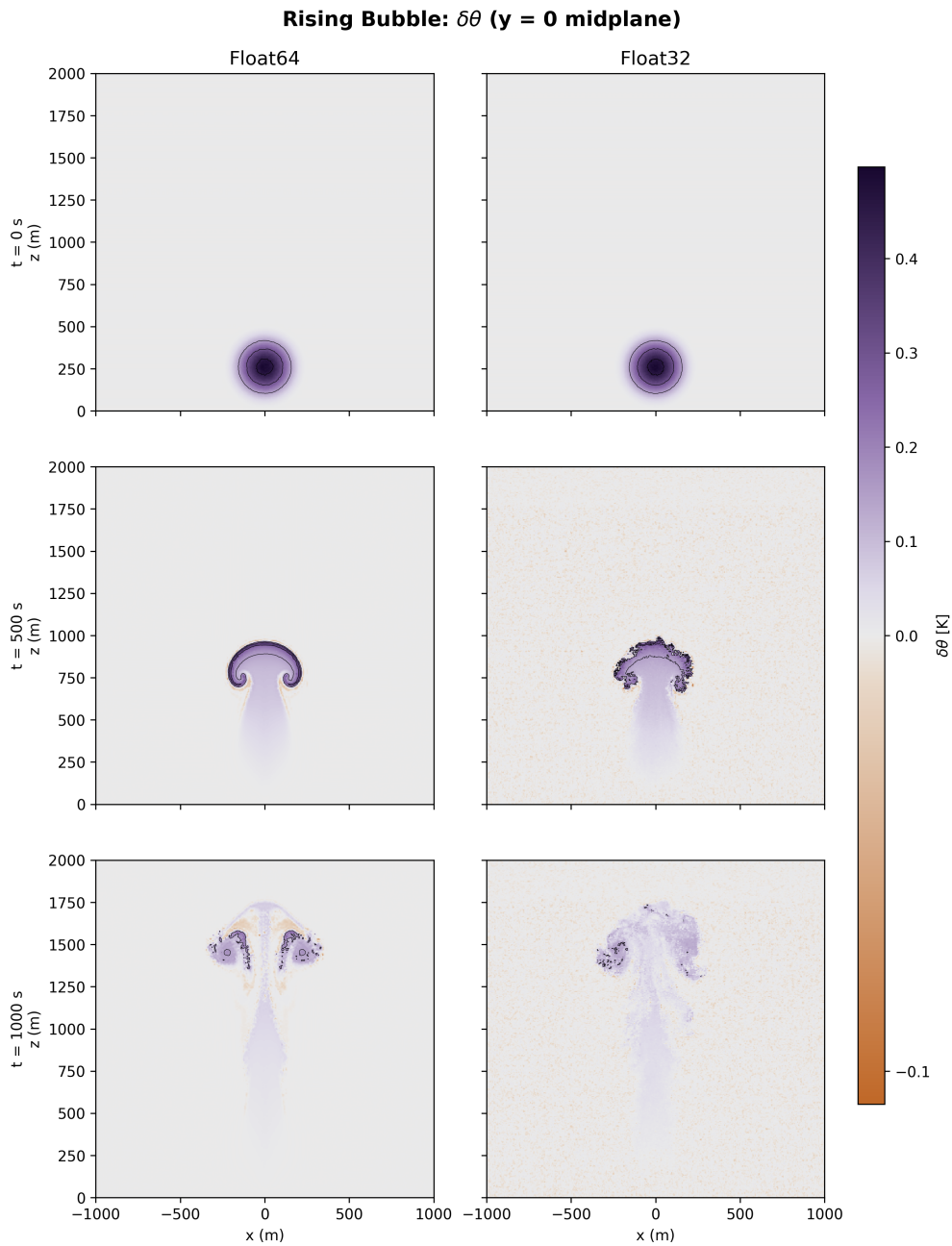


Figure 8: Slices of simulation results for potential temperature at $y = 0$ with $N = 4$, $L = 6$, and one coarse element in 64-bit (left) and 32-bit (right) precision. This simulation uses the smooth initial perturbation defined in (8).

order, $L = 3$ refinement level, and $K_x = 12$ coarse elements in the x direction, $K_y = 2$ in y , and $K_z = 1$ in z . This results in 1,536,000 DOF and an approximately 83 km resolution in x , 75 km resolution in y , and a 750 m resolution in z . We ran this with a time step of $\Delta t = 2.0$ s (Courant number $C \approx 1.05$) We plot these results in Figure 9 and see that they are qualitatively the same as those from [53]. We also compare these results with the NUMA model [24, 23]. The NUMA result shown in Fig. 9b uses a different equation set (potential temperature for thermodynamics), spectral elements, horizontally-explicit-vertically (HEVI) 2nd order additive Runge-Kutta time-integration, and 4th order hyper-viscosity; in sum, it represents the best solution we can provide within our collection of existing and published codes. The ESDG results compare well with the NUMA results even though it neither uses artificial dissipation nor benefits from a highly stable time-stepping approach.

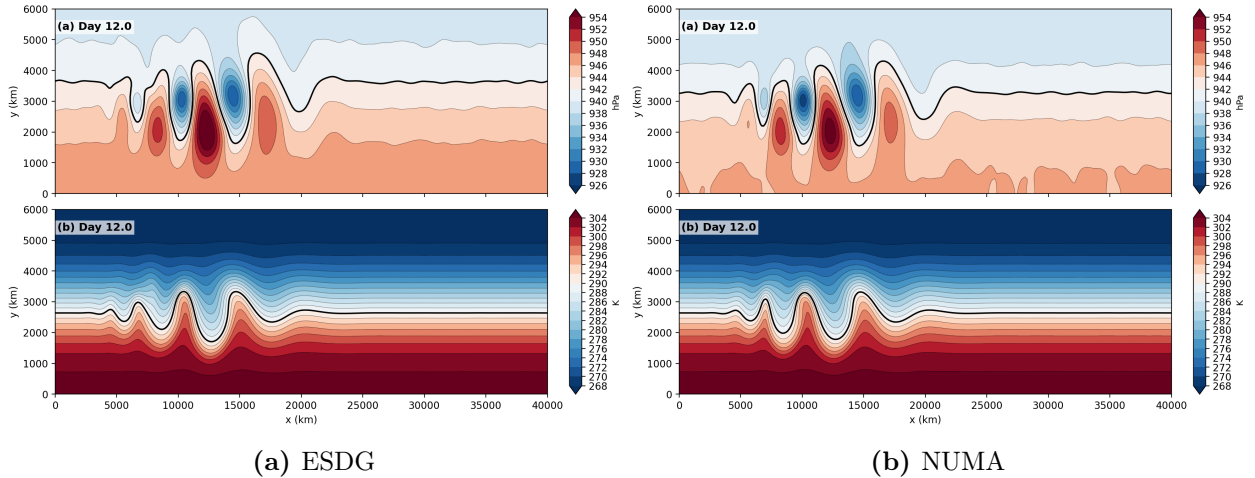


Figure 9: Slice at $z = 500$ m of pressure (Top) and temperature (Bottom) on day 12 for (a) ESDG and (b) NUMA. Simulation ran with $N = 4$, $L = 3$ and $K_x = 12$, $K_y = 2$, $K_z = 1$.

As in the rising bubble case, we compare performance in 32-bit and 64-bit precision. We summarize the timing results in Table 3 and the visual results in Figure 10 and Figure 11. We see that the 32-bit precision solution captures the same dynamics as the 64-bit precision solution with a small amount of noise which we attribute to the large magnitude of ρe . Global conservation of mass and total energy is verified by tracking $\sum_K \int_K \rho dV$ and $\sum_K \int_K \rho e dV$ over time; relative variations remain at machine precision for 32-bit ($\sim 10^{-7}$) and 64-bit precision ($\sim 10^{-15}$). Despite these conservation metrics we see visual noise in the 32-bit pressure plot. This is most likely due to our code working with the full state variables as opposed to perturbations. Carrying perturbation variables would allow the 32-bit precision more accuracy in small relative changes in the conserved variables, but the trade-off is additional storage and arithmetic for handling the reference state.

Table 3 shows that there is a tradeoff between speed and accuracy – we get a $1.5\times$ speedup going from 64-bit to 32-bit precision. This is less than the $2.16\times$ speedup we saw in the rising bubble case and this is primarily because of the ratio of computation to communication. Both simulations ran with 8 GPUs but the rising bubble case had a DOF count of 32,768,000 while the baroclinic instability has a significantly smaller DOF count of 1,536,000. This means that the communication overhead is a larger factor of the total

runtime and therefore computational speedups like switching precision will have less of an overall effect. By raising the GPU utilization through increasing number of elements or polynomial order, we could increase this speedup ratio. We prove this by increasing the size of the problem to $N = 4$, $L = 3$, $K_x = 36$, $K_y = 6$, $K_z = 3$ (41,472,000 DOFs), decreasing the timestep to $\Delta t = 0.5$, and running for a day. The coarse and fine timing results are listed in Table 3. We see that the fine results capture the same $2.16\times$ speedup as in the rising bubble case.

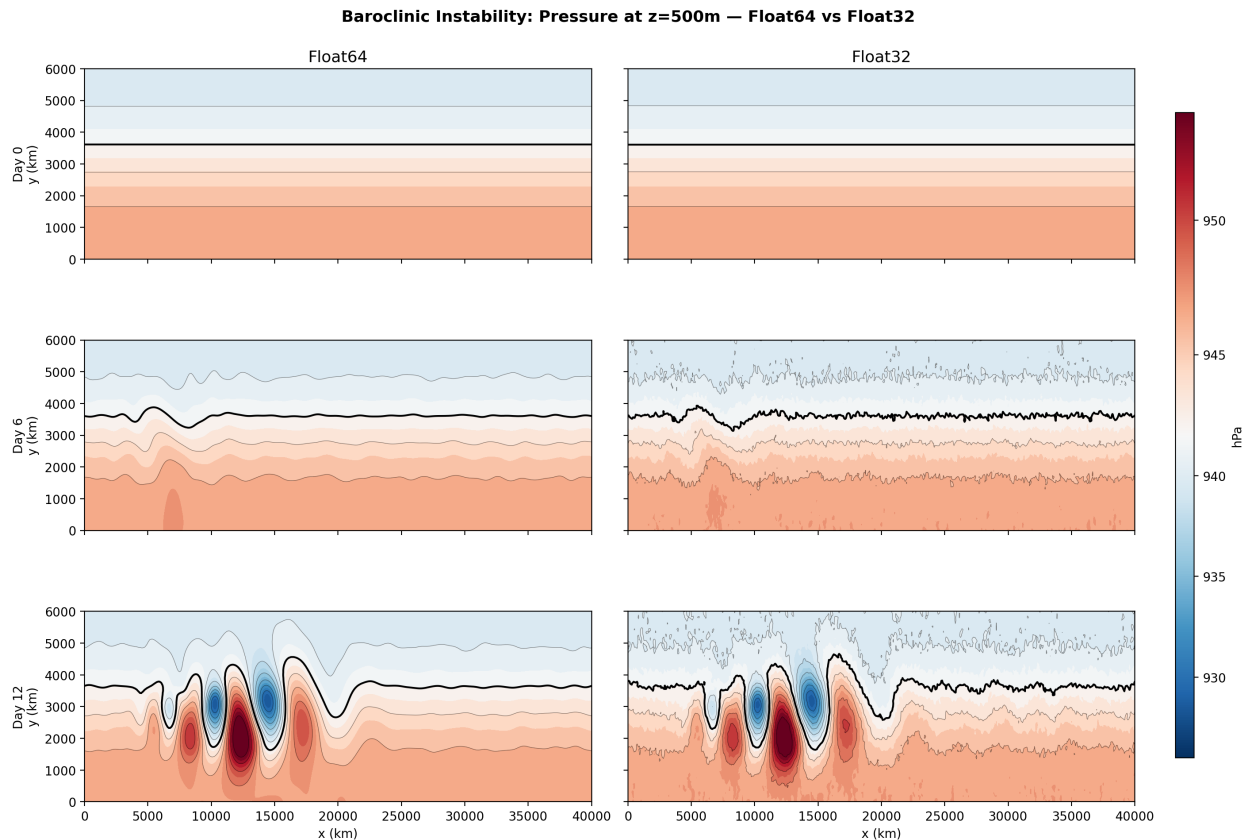


Figure 10: Slices of simulation results at $z = 500$ m of pressure at days 0, 6, and 12, in 64-bit (left) and 32-bit (right) precision. Simulation ran with $N = 4$, $L = 3$ and $K_x = 12$, $K_y = 2$, $K_z = 1$.

6. Conclusions

We presented a GPU implementation of the entropy-stable discontinuous Galerkin method for compressible Euler equations with buoyancy. We demonstrated the performance of the solver on two three-dimensional problems showing that, on NVIDIA A100 hardware, the solver achieves nearly 70% of 64-bit floating-point peak performance for the most computationally expensive kernel (volume terms) and that the optimized volume kernel significantly reduces the computational overhead typically incurred by two point entropy-stable fluxes. We also showed impressive strong and weak scaling performance of the solver and compared against a highly-optimized CPU code showing that the GPU kernels are a factor of $10\times$ faster and better than $13\times$ more energy efficient than the CPU code.

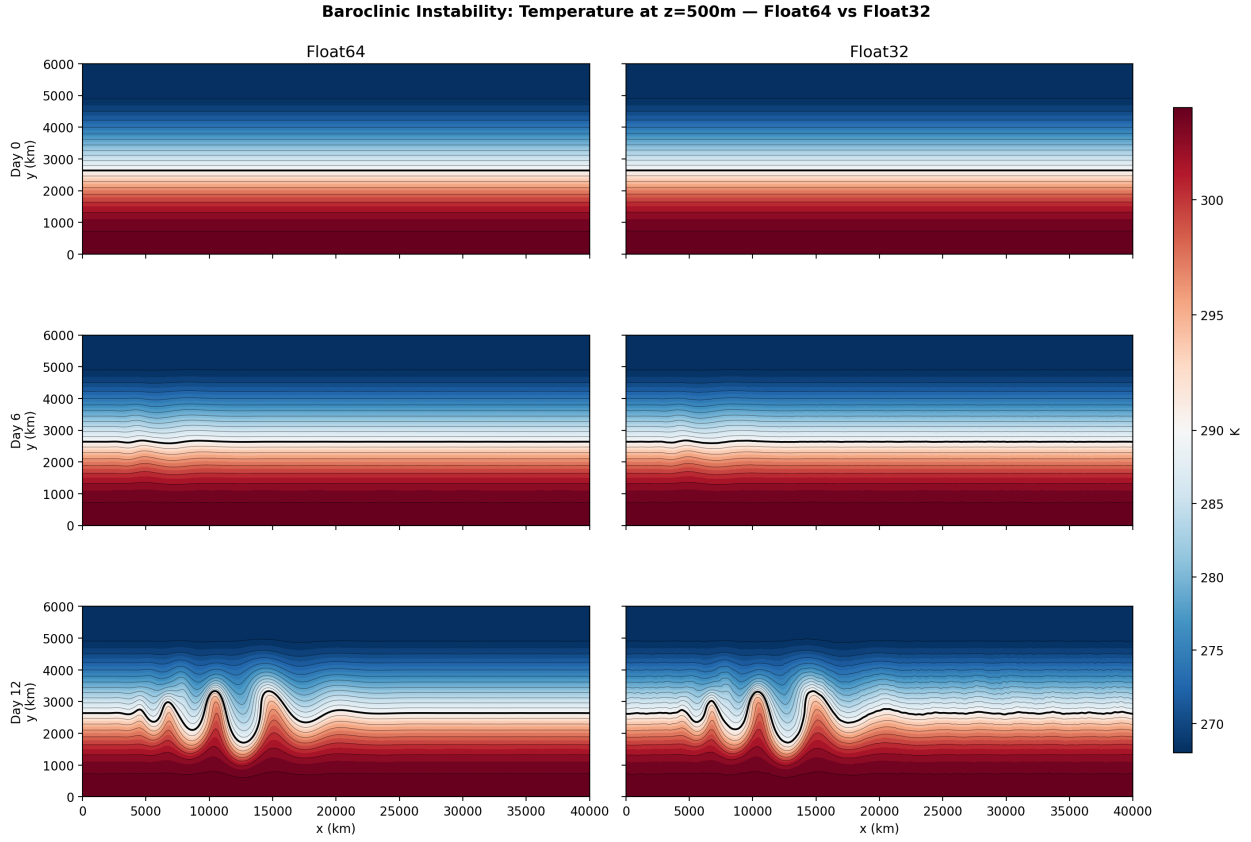


Figure 11: Slices of simulation results at $z = 500$ m of temperature at days 0, 6, and 12 in 64-bit (left) and 32-bit (right) precision. Simulation ran with $N = 4$, $L = 3$ and $K_x = 12$, $K_y = 2$, $K_z = 1$.

Table 3: Timing results for the baroclinic instability problem with both coarse (for 12 days) and fine (for a single day) configurations run on 8 GPUs

Size	Precision	Total Time [s]	Speedup
Coarse	64-bit	2611.57	—
	32-bit	1743.91	1.5×
Fine	64-bit	12442.62	—
	32-bit	5749.48	2.16×

We discussed different modifications implemented to reach this level of performance and reported on the performance gains of each of the implementation strategies ranging from reduction in complex operations and memory traffic as well as load balancing. We only used explicit time-integration because we wanted to focus on the performance of the ESDG spatial discretization; however, for a practical atmospheric model it is imperative to extend (at a minimum) to horizontally explicit vertically implicit methods (see, e.g., [49, 23]).

Acknowledgments

Waruszewski, Wilcox, and Giraldo were supported by the generosity of Eric and Wendy Schmidt by recommendation of the Schmidt Futures program. Waruszewski, Wilcox, and Giraldo were also supported by the National Science Foundation under grant AGS-1835881. Giraldo was also supported by Office of Naval Research Marine Meteorology and Space Weather program under grant N0001419WX00721. Sandia National Laboratories is a multimission laboratory managed and operated by National Technology & Engineering Solutions of Sandia, LLC, a wholly owned subsidiary of Honeywell International Inc., for the U.S. Department of Energy’s National Nuclear Security Administration under contract DE-NA0003525. This paper describes objective technical results and analysis. Any subjective views or opinions that might be expressed in the paper do not necessarily represent the views of the U.S. Department of Energy or the United States Government. This work used Delta at the National Center for Supercomputing Applications through allocation MTH250049 from the Advanced Cyberinfrastructure Coordination Ecosystem: Services & Support (ACCESS) program, which is supported by U.S. National Science Foundation grants #2138259, #2138286, #2138307, #2137603, and #2138296.

References

- [1] D. S. ABDI, F. X. GIRALDO, E. M. CONSTANTINESCU, L. E. CARR, L. C. WILCOX, AND T. C. WARBURTON, Acceleration of the implicit-explicit nonhydrostatic unified model of the atmosphere on manycore processors, *The International Journal of High Performance Computing Applications*, 33 (2017), pp. 242–267.
- [2] D. S. ABDI, L. C. WILCOX, T. C. WARBURTON, AND F. X. GIRALDO, A GPU-accelerated continuous and discontinuous Galerkin non-hydrostatic atmospheric model, *The International Journal of High Performance Computing Applications*, 33 (2017), pp. 81–109.
- [3] L. BERTAGNA, M. DEAKIN, O. GUBA, D. SUNDERLAND, A. M. BRADLEY, I. K. TEZAUER, M. A. TAYLOR, AND A. G. SALINGER, HOMMEXX 1.0: a performance-portable atmospheric dynamical core for the Energy Exascale Earth System Model, *Geoscientific Model Development*, 12 (2019), pp. 1423–1441.
- [4] T. BESARD, C. FOKET, AND B. DE SUTTER, Effective extensible programming: Unleashing Julia on GPUs, *IEEE Transactions on Parallel and Distributed Systems*, (2018).

- [5] J. BEZANSON, A. EDELMAN, S. KARPINSKI, AND V. B. SHAH, Julia: A fresh approach to numerical computing, *SIAM Review*, 59 (2017), pp. 65–98.
- [6] A. R. BRODTKORB AND M. L. L. SAETRA, Simulating the Euler equations on multiple GPUs using Python, *Frontiers In Physics*, 10 (2022).
- [7] C. BURSTEDDE, L. C. WILCOX, AND O. GHATTAS, p4est: Scalable algorithms for parallel adaptive mesh refinement on forests of octrees, *SIAM Journal on Scientific Computing*, 33 (2011), pp. 1103–1133.
- [8] S. BYRNE, L. C. WILCOX, AND V. CHURAVY, MPI.jl: Julia bindings for the Message Passing Interface, in *Proceedings of the JuliaCon Conferences*, vol. 1, 2021, p. 68.
- [9] M. H. CARPENTER AND C. A. KENNEDY, Fourth-order 2N-storage Runge-Kutta schemes, Technical Memorandum NASA TM-109112, National Aeronautics and Space Administration, Langley Research Center, Hampton, VA, 1994.
- [10] M. J. CASTRO, U. S. FJORDHOLM, S. MISHRA, AND C. PARES, Entropy conservative and entropy stable schemes for nonconservative hyperbolic systems, *SIAM Journal on Numerical Analysis*, 51 (2013), pp. 1371–1391.
- [11] M. CERNETIC, V. SPRINGEL, T. GUILLET, AND R. PAKMOR, High-order discontinuous Galerkin hydrodynamics with sub-cell shock capturing on GPUs, *Monthly Notices of the Royal Astronomical Society*, 522 (2023), pp. 982–1008.
- [12] —, Supersonic turbulence simulations with GPU-based high-order discontinuous Galerkin hydrodynamics, *Monthly Notices of the Royal Astronomical Society*, 534 (2024), pp. 1963–1984.
- [13] J. CHAN, Skew-symmetric entropy stable modal discontinuous Galerkin formulations, *Journal of Scientific Computing*, 81 (2019), pp. 459–485.
- [14] J. CHAN AND L. C. WILCOX, On discretely entropy stable weight-adjusted discontinuous Galerkin methods: curvilinear meshes, *Journal of Computational Physics*, 378 (2019), pp. 366–393.
- [15] T. CHEN AND C.-W. SHU, Entropy stable high order discontinuous Galerkin methods with suitable quadrature rules for hyperbolic conservation laws, *Journal of Computational Physics*, 345 (2017), pp. 427–461.
- [16] E. ELSEN, P. LEGRESLEY, AND E. DARVE, Large calculation of the flow over a hypersonic vehicle using a GPU, *Journal of Computational Physics*, 227 (2008), pp. 10148–10161.
- [17] T. C. FISHER AND M. H. CARPENTER, High-order entropy stable finite difference schemes for nonlinear conservation laws: Finite domains, *Journal of Computational Physics*, 252 (2013), pp. 518–557.

- [18] L. FRIEDRICH, A. R. WINTERS, D. C. D. R. FERNANDEZ, G. J. GASSNER, M. PARSANI, AND M. H. CARPENTER, An entropy stable h/p non-conforming discontinuous Galerkin method with the Summation-by-Parts property, *Journal of Scientific Computing*, 77 (2018), pp. 689–725.
- [19] M. FUHRY, A. GIULIANI, AND L. KRIVODONOVA, Discontinuous Galerkin methods on graphics processing units for nonlinear hyperbolic conservation laws, *International Journal For Numerical Methods In Fluids*, 76 (2014), pp. 982–1003.
- [20] G. J. GASSNER, A. R. WINTERS, AND D. A. KOPRIVA, Split form nodal discontinuous Galerkin schemes with summation-by-parts property for the compressible Euler equations, *Journal of Computational Physics*, 327 (2016), pp. 39–66.
- [21] F. X. GIRALDO, Trajectory calculations for spherical geodesic grids in Cartesian space, *Monthly Weather Review*, 127 (1999), pp. 1651–1662.
- [22] —, An Introduction to Element-based Galerkin Methods on Tensor-Product Bases - Analysis, Algorithms, and Applications, vol. 24, Springer, 2020.
- [23] F. X. GIRALDO, F. A. DE BRAGANÇA ALVES, J. F. KELLY, S. KANG, AND P. A. REINECKE, A performance study of horizontally explicit vertically implicit (HEVI) time-integrators for non-hydrostatic atmospheric models, *Journal of Computational Physics*, 515 (2024), p. 113275.
- [24] F. X. GIRALDO, J. F. KELLY, AND E. M. CONSTANTINESCU, Implicit-explicit formulations of a three-dimensional nonhydrostatic unified model of the atmosphere (NUMA), *SIAM Journal on Scientific Computing*, 35 (2013), pp. B1162–B1194.
- [25] F. X. GIRALDO AND M. RESTELLI, A study of spectral element and discontinuous Galerkin methods for the Navier–Stokes equations in nonhydrostatic mesoscale atmospheric modeling: equation sets and test cases, *Journal of Computational Physics*, 227 (2008), pp. 3849–3877.
- [26] A. GIULIANI AND L. KRIVODONOVA, Adaptive mesh refinement on graphics processing units for applications in gas dynamics, *Journal of Computational Physics*, 381 (2019), pp. 67–90.
- [27] O. GUBA, M. A. TAYLOR, P. A. ULLRICH, J. R. OVERFELT, AND M. N. LEVY, The spectral element method (SEM) on variable-resolution grids: evaluating grid sensitivity and resolution-aware numerical viscosity, *Geoscientific Model Development*, 7 (2014), pp. 2803–2816.
- [28] J. HESTHAVEN AND T. WARBURTON, Nodal Discontinuous Galerkin Methods, Springer, New York, 2008.
- [29] J. F. KELLY AND F. X. GIRALDO, Continuous and discontinuous Galerkin methods for a scalable three-dimensional nonhydrostatic atmospheric model: limited-area mode, *Journal of Computational Physics*, 231 (2012), pp. 7988–8008.

- [30] Y.-J. KIM, F. X. GIRALDO, M. FLATAU, C.-S. LIOU, AND M. S. PENG, A sensitivity study of the Kelvin wave and the Madden-Julian Oscillation in aquaplanet simulations by the Naval Research Laboratory Spectral Element Atmospheric Model, *Journal of Geophysical Research-Atmospheres*, 113 (2008).
- [31] A. C. KIRBY AND D. J. MAVRIPLIS, GPU-accelerated discontinuous Galerkin methods: 30x speedup on 345 billion unknowns, in *2020 IEEE High Performance Extreme Computing Conference (HPEC)*, IEEE High Performance Extreme Computing Conference, IEEE, 2020. *IEEE High Performance Extreme Computing Conference (HPEC)*, ELECTR NETWORK, SEP 21-25, 2020.
- [32] D. KOPRIVA, Implementing Spectral Methods for Partial Differential Equations, Springer, New York, 2009.
- [33] D. A. KOPRIVA AND G. J. GASSNER, An energy stable discontinuous Galerkin spectral element discretization for variable coefficient advection problems, *SIAM Journal on Scientific Computing*, 36 (2014), pp. A2076–A2099.
- [34] D. A. KOPRIVA, A. R. WINTERS, M. BOHM, AND G. J. GASSNER, A provably stable discontinuous Galerkin spectral element approximation for moving hexahedral meshes, *Computers & Fluids*, 139 (2016), pp. 148–160.
- [35] F.-A. KUO, M. R. SMITH, C.-W. HSIEH, C.-Y. CHOU, AND J.-S. WU, GPU acceleration for general conservation equations and its application to several engineering problems, *Computers & Fluids*, 45 (2011), pp. 147–154.
- [36] M. KURZ, D. KEMPF, M. P. BLIND, P. KOPPER, P. OFFENHÄUSER, A. SCHWARZ, S. STARR, J. KEIM, AND A. BECK, GALÆXI: Solving complex compressible flows with high-order discontinuous Galerkin methods on accelerator-based systems, *Computer Physics Communications*, 306 (2025), p. 109388.
- [37] M. LEFEBVRE, P. GUILLEN, J.-M. LE GOUEZ, AND C. BASDEVANT, Optimizing 2D and 3D structured Euler CFD solvers on Graphical Processing Units, *Computers & Fluids*, 70 (2012), pp. 136–147.
- [38] A. MÜLLER, M. A. KOPERA, S. MARRAS, L. C. WILCOX, T. ISAAC, AND F. X. GIRALDO, Strong scaling for numerical weather prediction at petascale with the atmospheric model NUMA, *The International Journal of High Performance Computing Applications*, 2 (2019), pp. 411–426.
- [39] NVIDIA, CUDA C++ Programming Guide, Release 13.2.
- [40] M. PARSANI, M. H. CARPENTER, T. C. FISHER, AND E. J. NIELSEN, Entropy stable staggered grid discontinuous spectral collocation methods of any order for the compressible Navier-Stokes equations, *SIAM Journal on Scientific Computing*, 38 (2016), pp. A3129–A3162.

- [41] H. RANOCHA, M. SCHLOTTKE-LAKEMPER, J. CHAN, A. M. RUEDA-RAMIREZ, A. R. WINTERS, F. HINDENLANG, AND G. J. GASSNER, Efficient implementation of modern entropy stable and kinetic energy preserving discontinuous Galerkin methods for conservation laws, *ACM Transactions on Mathematical Software*, 49 (2023), pp. 1–30.
- [42] H. RANOCHA, M. SCHLOTTKE-LAKEMPER, J. CHAN, A. M. RUEDA-RAMÍREZ, A. R. WINTERS, F. HINDENLANG, AND G. J. GASSNER, Efficient Implementation of Modern Entropy Stable and Kinetic Energy Preserving Discontinuous Galerkin Methods for Conservation Laws, *ACM Transactions on Mathematical Software*, 49 (2023), pp. 1–30.
- [43] S. REDDY, M. WARUSZEWSKI, F. A. DE BRAGANCA ALVES, AND F. X. GIRALDO, Schur complement IMplicit-EXplicit formulations for discontinuous Galerkin non-hydrostatic atmospheric models, *Journal of Computational Physics*, 491 (2023), p. 112361.
- [44] F. RENAC, Entropy stable DGSEM for nonlinear hyperbolic systems in nonconservative form with application to two-phase flows, *Journal of Computational Physics*, 382 (2019), pp. 1–26.
- [45] P. ROE, Characteristic-based schemes for the Euler equations, *Annual Review of Fluid Mechanics*, 18 (1986), pp. 337–365.
- [46] J. ROMERO, J. CRABILL, J. E. WATKINS, F. D. WITHERDEN, AND A. JAMESON, ZEFR: A GPU-accelerated high-order solver for compressible viscous flows using the flux reconstruction method, *Computer Physics Communications*, 250 (2020).
- [47] M. SIEBENBORN AND V. SCHULZ, GPU accelerated discontinuous Galerkin methods for Euler equations and its adjoint, in *High Performance Computing Symposium 2013 (Hpc 2013) - 2013 Spring Simulation Multi-Conference (SPRINGSIM'13)*, F. Liu, K. Rupp, R. Phillips, and W. Thacker, eds., vol. 45 of *Simulation Series*, 2013, pp. 15–21. *High Performance Computing Symposium (HPC 2013) / Spring Simulation Multi-Conference (SpringSim '13)*, San Diego, CA, APR 07-10, 2013.
- [48] M. SIEBENBORN, V. SCHULZ, AND S. SCHMIDT, A curved-element unstructured discontinuous Galerkin method on GPUs for the Euler equations, *Computing and Visualization in Science*, 15 (2012), pp. 61–73.
- [49] A. N. SOUZA, J. HE, T. BISCHOFF, M. WARUSZEWSKI, L. NOVAK, V. BARRA, T. GIBSON, A. SRIDHAR, S. KANDALA, S. BYRNE, L. C. WILCOX, J. E. KOZDON, F. X. GIRALDO, O. KNOTH, J. MARSHALL, R. FERRARI, AND T. SCHNEIDER, The flux-differencing discontinuous Galerkin method applied to an idealized fully compressible nonhydrostatic dry atmosphere, *Journal of Advances in Modeling Earth Systems*, 15 (2023), p. e2022MS003527.
- [50] F. SPORYKHIN AND H. HOMANN, Performance of a high-order MPI-Kokkos accelerated fluid solver, *Computer Physics Communications*, 318 (2026).

- [51] E. TADMOR, Numerical viscosity and the entropy condition for conservative difference-schemes, *Mathematics of Computation*, 43 (1984), pp. 369–381.
- [52] E. TADMOR AND W. ZHONG, Entropy stable approximations of Navier-Stokes equations with no artificial numerical viscosity, *Journal of Hyperbolic Differential Equations*, 3 (2006), pp. 529–559.
- [53] P. A. ULLRICH, K. A. REED, AND C. JABLONOWSKI, Analytical initial conditions and an analysis of baroclinic instability waves in f - and β -plane 3D channel models, *Quarterly Journal of the Royal Meteorological Society*, 141 (2015), pp. 2972–2988.
- [54] Y. WANG AND L. PAN, Three-dimensional discontinuous Galerkin based high-order gas-kinetic scheme and GPU implementation, *Computers & Fluids*, 242 (2022).
- [55] M. WARUSZEWSKI, J. E. KOZDON, L. C. WILCOX, T. H. GIBSON, AND F. X. GIRALDO, Entropy stable discontinuous Galerkin methods for balance laws in non-conservative form: Applications to the Euler equations with gravity, *Journal of Computational Physics*, 468 (2022).
- [56] A. WELTER AND N. C. NGUYEN, Preconditioning techniques for hybridizable discontinuous Galerkin discretizations on GPU architectures, *Computer Methods In Applied Mechanics And Engineering*, 456 (2026).
- [57] S. WILLIAMS, A. WATERMAN, AND D. PATTERSON, Roofline: An Insightful Visual Performance Model for Floating-Point Programs and Multicore Architectures, Tech. Rep. 1407078, Sept. 2009.
- [58] N. WINTERMEYER, A. R. WINTERS, G. J. GASSNER, AND T. WARBURTON, An entropy stable discontinuous Galerkin method for the shallow water equations on curvilinear meshes with wet/dry fronts accelerated by GPUs, *Journal of Computational Physics*, 375 (2018), pp. 447–480.
- [59] F. D. WITHERDEN, A. M. FARRINGTON, AND P. E. VINCENT, PyFR: An open source framework for solving advection-diffusion type problems on streaming architectures using the flux reconstruction approach, *Computer Physics Communications*, 185 (2014), pp. 3028–3040.
- [60] F. D. WITHERDEN, P. E. VINCENT, W. TROJAK, Y. ABE, A. AKBARZADEH, S. AKKURT, M. ALHAWWARY, L. CAROS, T. DZANIC, G. GIANGASPERO, A. S. IYER, A. JAMESON, M. KOCH, N. LOPPI, S. MISHRA, R. MODI, G. SAEZ-MISCHLICH, J. S. PARK, B. C. VERMEIRE, AND L. WANG, PyFR v2.0.3: Towards industrial adoption of scale-resolving simulations, *Computer Physics Communications*, 311 (2025).
- [61] X. WU, E. J. KUBATKO, AND J. CHAN, High-order entropy stable discontinuous Galerkin methods for the shallow water equations: Curved triangular meshes and GPU acceleration, *Computers & Mathematics With Applications*, 82 (2021), pp. 179–199.

- [62] J.-L. ZHANG, Z.-H. MA, H.-Q. CHEN, AND C. CAO, A GPU-accelerated implicit meshless method for compressible flows, *Journal of Computational Physics*, 360 (2018), pp. 39–56.